Fluid Dynamics in Conically Tapered Microneedles

Wijaya Martanto, Stephen M. Baisch, Elizabeth A. Costner, and Mark R. Prausnitz
School of Chemical & Biomolecular Engineering, Georgia Institute of Technology, Atlanta, GA 30332

Marc K. Smith
Woodruff School of Mechanical Engineering, Georgia Institute of Technology, Atlanta, GA 30332

DOI 10.1002/aic.10424
Published online April 21, 2005 in Wiley InterScience (www.interscience.wiley.com).

Toward achieving painless injections and other microfluidic applications, we microfabricated conically tapered needles of micron dimensions. The relationship between pressure drop and flow rate through microneedles was experimentally quantified as a function of fluid viscosity and microneedle length, diameter, and cone half-angle. At Reynolds numbers $\lesssim$ 100, dimensionless pressure drop ($2\Delta P/\rho v^2$) sharply decreased with increasing Reynolds number, indicating the importance of viscous forces. At larger Reynolds numbers, the flow was almost inviscid, as indicated by a weak dependency of dimensionless pressure drop on Reynolds number. Numerical simulations showed good agreement with experimental data and predicted that flow through conically tapered microneedles is primarily controlled by the diameter and taper angle at the microneedle tip. A characteristic feature of flow through conically tapered microneedles is a favorable axial pressure gradient that accelerates fluid through the microneedle, thus inhibiting growth of the viscous boundary layer on the microneedle wall. © 2005 American Institute of Chemical Engineers *AIChE J,* 51: 1599–1607, 2005
Keywords: microneedles, microfluidics, microfabrication, conical flow, drug delivery

Introduction

Advances in biotechnology and pharmaceuticals have led to sophisticated new drugs with potent and specific activity. However, these compounds are often difficult to deliver into the body using conventional methods.[1,2] Oral delivery is the most common way drugs are administered, but many compounds are either degraded in the gastrointestinal tract or liver, or are poorly absorbed across the intestine. When this occurs, the usual alternative is to use a hypodermic needle for injection across the skin, which avoids the enzymatic and diffusional barriers of oral delivery.

Hypodermic needle injection can easily and rapidly deliver large doses of drugs into the body, but its limitations include pain, expertise required for use, and difficulty to achieve sustained delivery.[3] To address these limitations, drug delivery by diffusion across skin from a transdermal patch has been developed.[4,5] As demonstrated by widespread use of the nicotine patch, this mode of delivery is relatively painless, easy to administer, and capable of long-term use. However, transdermal delivery is limited by the extremely poor permeability of human skin. The $2 billion worldwide patch market is based on just a dozen drugs that are able to cross skin at useful rates because of their favorable properties of low molecular weight, high oil solubility, and therapeutic value at low doses.[6]

Rather than avoid needles altogether, we have proposed a hybrid concept that captures the potential benefits of both hypodermic needles and transdermal patches, and may avoid each of their limitations. This concept involves micron-size needles that are sufficiently long to penetrate the outer permeability barrier of stratum corneum, but small enough to avoid stimulating nerves.[7,8] To demonstrate this approach, we previ-

Correspondence concerning this article should be addressed to M. R. Prausnitz at mark.prausnitz@chbe.gatech.edu.

ously created needles of micron dimensions using microfabrication technology involving photolithography and plasma etching of silicon wafers. Insertion of these microneedles into skin increased permeability for transdermal diffusion of small compounds, proteins, and nanoparticles by orders of magnitude.[9] Tests in human volunteers showed that microneedles inserted into the skin were painless.[10] Others have also studied fabrication and applications of solid microneedles.[11,12]

To extend microneedle capabilities to actively deliver drugs by convection, we more recently fabricated hollow microneedles that could be coupled with a pump or syringe for injection. Hollow microneedles were initially made by photolithography and plasma etching,[13] although our current approach involves laser drilling polymeric molds and electrodepositing metal onto the molds.[14] These microneedles have been shown to permit flow of fluid and insert into skin.[9,15] Others have also studied fabrication and applications of hollow microneedles.[16,17]

The pressure drop required to flow fluid through a microneedle depends on needle geometry and fluid viscosity and density. Needles of micron dimensions can exhibit significant resistance to flow. Measurement and prediction of microneedle fluid dynamics are needed to design needles that balance between geometries small enough to avoid pain, sharp enough to easily insert into skin, and large enough to permit useful flow rates at reasonable pressures. To address this need, this study sought to experimentally quantify the relationship between pressure drop and flow rate as a function of microneedle geometry and fluid viscosity, and to use computer simulations to model fluid dynamics in microneedles.

Flow through microneedles is characterized by (1) micron dimensions, (2) conically tapered channels, and (3) flow over a broad range of Reynolds numbers that can span at least 1–1000. To gain perspective from the literature, there are numerous studies of fluid flow inside microchannels,[18,19] but we are not aware of any that address flow through conically tapered geometries. Fluid flow through macroscopic conical channels has been addressed in the literature, but primarily for developed flow in long channels. Approximate analytical solutions have been derived for short channels with the assumption of creeping flow, limited contraction factor, and small taper angle,[20-23] which may not apply to microneedles.

These theoretical approaches have been validated macroscopically using only limited or no data and have not been validated at microscopic dimensions. The experimental data that do exist,[24] as well as the more extensive numerical analysis of fluids in conical channels,[25,26] is almost exclusively at low Reynolds numbers, where viscous effects dominate inertial effects. For this reason, our data can also be used to validate previous analytical and numerical predictions from the literature.

Experimental Methods

To quantify the relationship between applied pressure drop and flow rate as a function of microneedle geometry, polyester films (Mylar, DuPont Teijin Films, Wilmington, DE) were drilled using a 248-nm-wavelength UV Excimer Laser (ATLEX 300i, Resonetics, Nashua, NH) to create microneedle molds of defined length, inlet diameter, tip diameter, and cone half-angle.[14] The molds were then cleaned by wiping the surface with methanol (Sigma Aldrich, St. Louis, MO) to remove residual surface contamination from the laser drilling process. Mold dimensions were determined using a digital stereomicroscope (Quadra Chek 200, Metronics Inc., Bedford, NH). To account for imperfections in geometry, effective needle tip diameter was calculated based on the area of the needle bore at the tip, assuming a circular geometry (LSM 510 Image Browser, Zeiss, Oberkochen, Germany). Scanning electron micrographs of hollow microneedles and the polymer mold used to make a microneedle are shown in Figure 1.

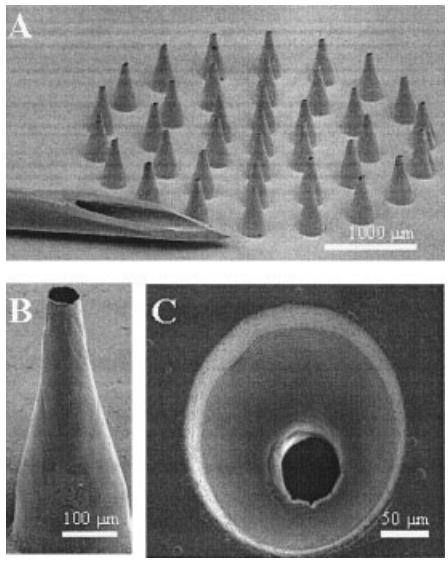

Figure 1. Scanning electron micrographs of hollow microneedles.

(A) An array of microneedles is shown next to the tip of a 30-gauge hypodermic needle. (B) A single microneedle is shown from a side view. (C) The polymer mold used to make that needle is shown from above. Needle and mold dimensions are needle length $L_n = 500$ μm, inlet diameter $D_i = 220$ μm, tip diameter $D_t = 56$ μm, and cone half-angle $\theta_c = 9°$.

To simplify the experimental protocol, fluid flow measurements were not made on microneedles, but were made on the molds used to fabricate microneedles. Although details of surface properties and orifice geometries differ between polymer molds and metal needles, we expect that molds and needles having the same internal geometry will still produce similar flow fields when given the same pressure drop.

The fluids used in this study were filtered deionized water, glycerin solutions, and bovine calf blood (in Alsevers anticoagulant, Rockland Immunochemicals, Gilbertsville, PA). The pressure drop measurement for deionized water was performed at room temperature (~22°C). Because the viscosity of glycerin solutions and blood is sensitive to temperature, studies with these fluids were performed in controlled-temperature rooms (4°C for glycerin solutions and 37°C for blood to model body temperature). Glycerin solutions were prepared by mixing filtered deionized water with glycerin (Fisher Scientific, Suwanee, GA) to yield 0, 7, 36, and 48 wt % glycerin solutions.

The viscosity (Cannon Ubbelohde viscometer, Cannon Instrument, State College, PA) and density (BP 210S digital balance, Sartorius, Goettingen, Germany) of the glycerin solutions with increasing glycerin content were determined at 4°C to be 1.0, 2.1, 5.1, and 9.8 mPa·s and 1.00, 1.00, 1.06, and

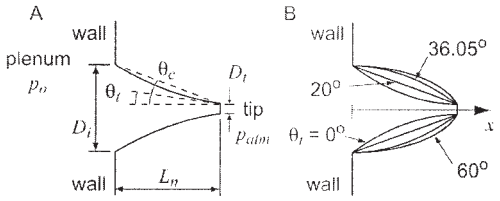

Figure 2. (A) Idealized microneedle geometry with relevant dimensions and angles: cone half-angle θ_c, tip angle θ_t, tip diameter D_t, inlet diameter D_i, and needle length L_n (the flow enters the microneedle from the left originating from a large plenum chamber held at a pressure of p_0; the flow exits at the tip to the local atmosphere held at a constant pressure of p_{atm}); (B) microneedle wall profiles for a cone half-angle θ_c = 20°, a dimensionless length L = 10, and four tip angles θ_t = 0, 20, 36.05, and 60°.

The tip angle $\theta_t = 36.05°$ is the transition angle θ_p marking the transition from a parabolic profile to an elliptic profile.

1.12×10^3 kg/m^3, respectively. Viscosity and density of deionized water at 22°C was 1.0 mPa·s and 998 kg/m^3, respectively, and blood at 37°C was 1.7 mPa·s and 1.04×10^3 kg/m^3, respectively. Although blood exhibits non-Newtonian behavior, comparison with previous measurements suggests that this viscosity value is representative over the range of shear rates encountered in this study[27] (1.3×10^3–6.9×10^4 s^{-1}).

Pressure drop measurements were performed by flowing the solution of interest at a constant flow rate from a syringe pump (Genie YA-12, Kent Scientific, Torrington, CT) past a digital pressure gauge (Merigauge 3900-GI0100, Meriam Instrument, Cleveland, OH) and through microneedle molds. The lower limit of flow rate used in the study was determined by the minimum flow rate at which a continuous liquid jet was formed (that is, not discrete droplets). The upper limit was determined by the flow rate at the maximum pressure produced by our pump (that is, 284 kPa). Measurements for each needle geometry were performed at least in triplicate.

To compare the predictive ability of models to experimental data, we determined the mean absolute percent error (MAPE) associated with differences between predicted and measured dimensionless pressure drop values, defined as the average absolute value of the difference divided by the experimental value

$$\text{MAPE} = \frac{|\Delta P_{\text{predicted}} - \Delta P_{\text{measured}}|}{\Delta P_{\text{measured}}} \times 100\% \tag{1}$$

where ΔP is the dimensionless pressure drop across the microneedle (predicted or measured).

Numerical Simulation of Fluid Flow in a Microneedle

To determine the pressure drop across a microneedle as a function of flow rate and microneedle geometry, a series of computational fluid dynamics simulations were done using the geometry shown in Figure 2A. Fluid enters the left side of the microneedle from a large plenum and exits through the tip at the right. The geometry is axisymmetric and the microneedle has a curved profile characterized by four parameters: the tip diameter D_t, inlet diameter D_i, length L_n, and tip angle θ_t. From these, the cone half-angle θ_c is defined as

$$\theta_c = \arctan\left(\frac{D_i - D_t}{2L_n}\right) \tag{2}$$

The curved profile typical of our conically tapered microneedles (see Figure 2) was mathematically modeled using either a parabola or an ellipse, parameterized mainly by the tip angle θ_t. The transition between these two shapes occurs at the transition tip angle $\theta_p = \arctan[2 \tan(\theta_c)]$. Thus, the microneedle profile was that of a parabola, ellipse, or straight-sided cone when the tip angle satisfied the relations $0 \le \theta_t \le \theta_p$, $\theta_t > \theta_p$, or $\theta_t = \theta_c$, respectively. Examples of each of these profiles are shown in Figure 2B. The tip diameter was used to scale the geometric parameters and so three dimensionless parameters uniquely define this geometry: the dimensionless length $L = L_n/D_t$, the cone half-angle θ_c, and the microneedle tip angle θ_t.

The flow model was axisymmetric, steady, incompressible, laminar, and Newtonian. The viscosity μ and density ρ of the fluid were constant. The curved inlet to the flow domain in the large plenum chamber to the left of the microneedle (not shown in Figure 2A) was held at the constant pressure p_0. The flow outlet at the tip was held at a constant atmospheric pressure p_{atm}. Two dimensionless groups characterize the flow in the microneedle: the Reynolds number,

$$\text{Re} = \frac{\rho \bar{V} D_t}{\mu} \tag{3}$$

and the dimensionless pressure drop,

$$\Delta P = \frac{p_0 - p_{atm}}{1/2(\rho \bar{V}^2)} \tag{4}$$

where $\bar{V}$ is the average velocity at the microneedle tip.

The simulations were done using the computational fluid dynamics software FLUENT (version 6.0, Lebanon, NH). The dimensionless parameters describing the geometry of the microneedle—the length L, tip angle θ_t, and cone half-angle θ_c—were varied over a wide range that included all experimental values. For each microneedle profile, approximately 100 different flow rates were simulated so that the Reynolds number varied over the range $0 \le \text{Re} \le 1000$. The plenum size was selected as two inlet diameters along the microneedle axis and along the wall, which was large enough so that the pressure drop and mass flow rate through the needle were independent of plenum size. Similarly, the mesh size selected was 80 elements per unit length in the microneedle, which was large enough that the flow simulations were independent of mesh size. The results reported here are accurate to <0.6% uncertainty for Re < 1, and the error rises to about 3% for Re = 1000.

Results

To determine whether needles of micron dimensions can be used to transfer fluids for injecting drug solutions into skin or for other microfluidic applications, we flowed liquids through microneedle molds and measured the pressure drop required as a function of microneedle geometry and fluid viscosity. Conically tapered microneedle molds used in this study were laser drilled using microfabrication techniques, as shown in Figure 1.

Measurement of pressure drop vs. flow rate

One of the goals for this study was to quantify the relationship between flow rate and pressure drop as a function of microneedle geometry. We made these measurements using 22 different needle geometries each at 4–7 different flow rates for a total of 153 measurements. The range of geometries considered spanned inlet diameters of D_i = 102–412 μm, tip diameters of D_t = 20–96 μm, cone half-angles of θ_c = 5–20°, and lengths of L_n = 100–500 μm.

Figure 3A shows the raw data measured from a representative set of individual microneedles (each having the same cone half-angle, but different diameters and lengths). It shows that pressure drop increased in a nonlinear manner with increasing flow rate and with decreasing tip diameter D_t. For this representative set of microneedle geometries, only modest pressures were required to achieve flow rates of many microliters per second per needle, which may be of interest for drug delivery applications. Over the full range of microneedle geometries considered, pressure drops of 4.6–196.5 kPa were required to achieve flow rates of 1.4–56 μL/s.

Nondimensionalized data for all 22 microneedle geometries tested are shown together as dimensionless pressure drop ΔP vs. Reynolds number Re in Figure 3B. Albeit with some scatter, the data collapse into a set of similar curves, which show the characteristic transition from a viscously dominated flow at small Reynolds number, where dimensionless pressure decreases inversely with Reynolds number, to an inertially dominated flow at large Reynolds number, where dimensionless pressure is relatively independent of Reynolds number. Most data were generated using water as the fluid, but a subset of data points used water—glycerin solutions with elevated viscosity (1–9.8 mPa·s) or blood (1.7 mPa·s).

Comparison of experimental data to theoretical predictions from literature

Another goal of this study was to determine whether theoretical expressions developed in previous studies that modeled flow through conical channels could predict our experimental measurements in microneedles. We identified three theoretical approaches and one numerical simulation that are representative of the scope of published literature on this topic.

The three theoretical approaches showed varying levels of agreement with our experimental measurements. Kemblowski and Kiljanski[24] modeled fluid flow through a conical geometry by assuming that the axial velocity profile at each axial location was similar to the Poiseuille velocity profile for flow in a circular tube. This model is most valid in the slow-flow limit, where Re $<$ 1, and for small cone half-angles. It yielded a MAPE value of 52%, meaning that predictions were on average within ±52% of our experimental values. Nishimura and Oka[22] computed an approximate solution to the flow equations in a conical geometry using a series expansion of the velocity based on inverse powers of the radial distance from the virtual vertex of the cone. This solution produced a small inertial correction to the flow field, but they showed that this correction did not influence the flow rate. Thus, their result is equivalent to the slow-flow limit, and it yielded a MAPE value of 67%. Both of these flow models are most accurate in the small-Reynolds-number limit Re $<$ 1, and this explains their failure to accurately predict our data, which lies in the Reynolds number range 28 $<$ Re $<$ 1000.

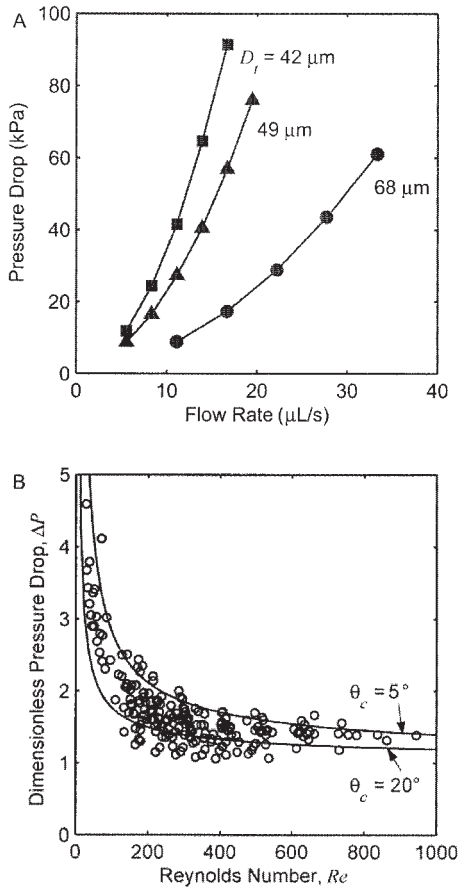

Figure 3. (A) Pressure drop required for flow of water through representative microneedles of different geometries as a function of flow rate (three different needle geometries, each with the same cone half-angle, θ_c = 15°, but with different tip diameter (D_t), inlet diameter (D_i), and length (L_n) are compared: (■) D_t = 42 μm, D_i = 162 μm, L_n = 225 μm; (▲) D_t = 50 μm, D_i = 322 μm, L_n = 500 μm; (●) D_t = 68 μm, D_i = 342 μm, L_n = 500 μm); (B) the dimensionless pressure drop vs. Reynolds number for flow in conical microneedles.

The circles mark all experimental data points. The two solid lines are the results from numerical simulations for straight-sided cones with dimensionless length L = 10 and cone half-angles θ_c = 5 and 20°. Each data point represents the mean of at least three measurements; standard deviation error bars are contained within the data points.

In contrast, Sutterby[21] developed an equation for the pressure drop in a non-Newtonian conical flow by simply adding the relevant numerical solution in the slow-flow limit with the inviscid solution in the large-Reynolds-number limit. This approach, which yielded a MAPE value of 30%, worked better than the previous two approaches because most of our data lies in the large-Reynolds-number range where inertial forces dominate the flow. Jarzebski and Wilkinson[25] performed a finite-difference solution of the governing equations of motion for the flow in a tapered tube with a parabolic velocity profile at the entrance. They used the result to develop a pressure-drop correlation based on the Stokes-flow solution of Harrison.[28] The correlation was within 5% of their numerical results for Reynolds numbers < 750 and cone half-angles $< 7°$. The approach yielded a MAPE value of 48% with respect to our data. It did not perform as well as Sutterby's result because the cone half-angle in our microneedles was in the range $5° < \theta_c < 21°$ and because of the different entrance geometry and flow present in our experiments.

Numerical simulation of fluid flow in a microneedle

To further study the effects of microneedle geometry on the dynamics of flow through a microneedle, we developed a model appropriate for our experimental conditions and performed numerical simulations over a broad range of conditions to produce curves expressing the dimensionless pressure drop ΔP as a function of the Reynolds number Re, with the dimensionless length L, cone half-angle θ_c, and tip angle θ_t as parameters. In our first set of results, microneedles were modeled as straight-sided cones with cone half-angles ranging from $\theta_c = 5°$ to $\theta_c = 20°$, as determined from experimental measurements of microneedle geometry (see above). Figure 3B shows all of the experimental data together with the predicted dimensionless pressure drop vs. Reynolds number curves for the smallest and largest cone half-angles. These numerical curves approximately bound the experimental data. A more quantitative assessment of the simulation's predictive ability was produced by comparing errors between each individual predicted data point and its corresponding measured value, which yielded a MAPE value of 11% for the whole data set.

Effect of microneedle length L

Simulation results were next used to predict the effect of microneedle geometry on dimensionless pressure drop at different Reynolds numbers in greater detail. The effect of needle length was considered first. As a base case, the dimensionless pressure drop for a cylindrical microneedle (that is, not tapered, $\theta_c = 0$) is shown at four different lengths in Figure 4A. The dimensionless pressure drop decreases monotonically with Reynolds number and increases with length. As $\mathrm{Re} \to 0$, each curve approaches the well-known, Hagen–Poiseuille result of $\Delta P = fL = (64/\mathrm{Re})L$ for fully developed, laminar pipe flow, where f is the Darcy friction factor.[29] As $\mathrm{Re} \to \infty$, all curves approach the limiting value of one for purely inviscid flow. However, for Reynolds numbers as large as 1000, the dimensionless pressure drop continues to vary with length and is significantly greater than the purely inviscid result, which is attributed to the developing entrance flow in these microneedles. The dimensionless distance required to establish a

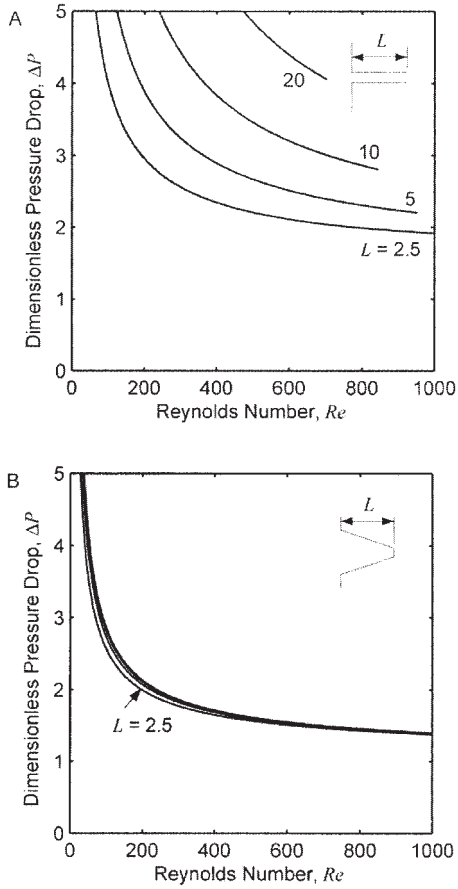

Figure 4. Effect of microneedle length on dimensionless pressure drop vs. Reynolds number.

The geometries are (A) a circular cylinder with $\theta_c = 0°$ and (B) a tapered, straight-sided cone with $\theta_c = 5°$ having dimensionless lengths $L = 2.5$, 5, 10, and 20. In (B), the three curves for dimensionless length $L \geq 5$ are almost indistinguishable.

fully developed, laminar flow in a cylindrical pipe is the dimensionless entrance length[29] $L_e^* = L_e/D_t = 0.06\mathrm{Re}$. For $\mathrm{Re} = 1000$, the entrance length is $L_e^* = 60$, which is three times longer than the longest needle considered ($L = 20$). Thus, the large Reynolds number behavior in Figure 4A is attributed to the developing boundary layer in the needle.

In contrast to cylindrical microneedles, there is very little effect of needle length on flow through microneedles with tapered sides (Figure 4B). Tapered microneedles are of interest because their sharper tips permit easier insertion into skin.[15] Figure 4B shows the results for a cone-shaped microneedle with a straight-sided taper ($\theta_t = \theta_c$), a cone half-angle $\theta_c = 5°$, and four different lengths. There is still a significant variation in the dimensionless pressure drop with Reynolds number, but the dependency on needle length L is small. At larger cone half-angles, the curves for the four different lengths are indistinguishable (data not shown). The reason that dimensionless pressure drop in tapered needles is largely independent of needle length L is discussed below.

Effect of cone half-angle θ_c and tip angle θ_t

To assess the effect of cone half-angle θ_c on microneedle fluid dynamics, Figure 5A shows the dimensionless pressure

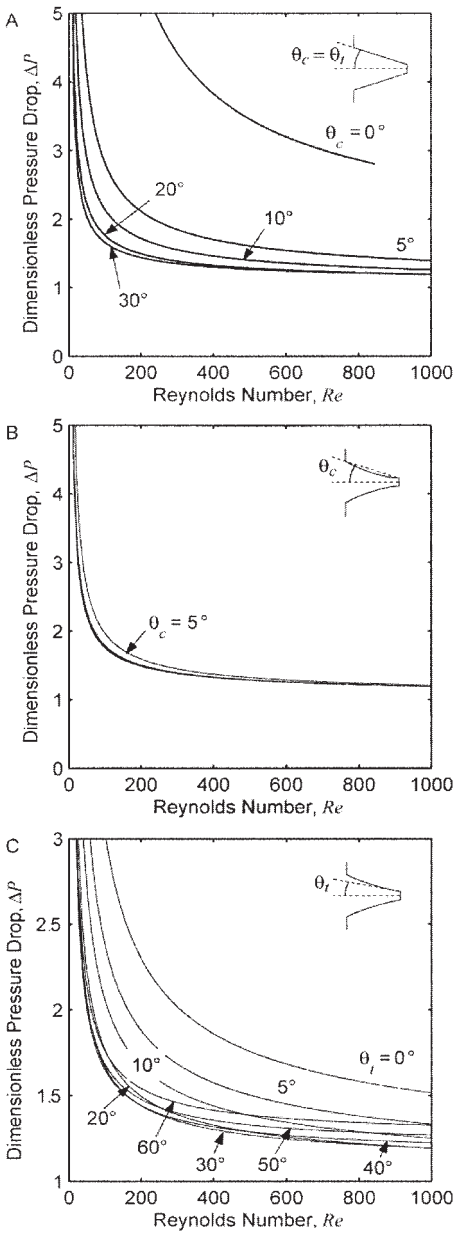

Figure 5. Effect of microneedle taper on dimensionless pressure drop vs. Reynolds number.

(A) The geometry is a straight-sided cone ($\theta_c = \theta_t$) with cone half-angles θ_c = 0, 5, 10, 20, and 30°. (B) The microneedle has a curved profile with cone half-angles θ_c = 5, 10, 20, and 30° and a fixed tip angle θ_t = 20°. The curves for the three larger cone half-angles are almost indistinguishable. (C) The microneedle has a curved profile with tip angles θ_t = 0, 5, 10, 20, 30, 40, 50, and 60° and a fixed cone half-angle θ_c = 20°. All geometries have a dimensionless length L = 10.

drop for microneedles with a straight-sided profile ($\theta_t = \theta_c$) and with various values for the cone half-angle θ_c. Because dimensionless pressure drop is almost independent of microneedle length for geometries of interest (that is, $\theta_c \geq 5°$), microneedle length was set to a representative value of $L = 10$. The simulations show that dimensionless pressure drop decreases with increasing Reynolds number and increasing cone half-angle, especially between $\theta_c = 0°$ (a straight cylinder) and $\theta_c = 5°$ (gently tapered).

The data from Figure 5A indicate that the cone half-angle for a straight-sided conical microneedle is an important parameter. However, the geometry of a straight-sided cone ($\theta_t = \theta_c$) is not representative of most microneedles used in this study, which have tapered sides with curved profiles (Figure 1B). To address this complexity, microneedle sidewall profiles were modeled as either parabolas or ellipses with a specified tip angle θ_t that could be varied independently from the cone half-angle θ_c, as described in the numerical methods section (see Figure 2). Tip angle is explicit in this model because of our expectation that most of the pressure drop occurs near the tip of the microneedle, which is validated and discussed below.

To decouple the effects of cone half-angle and needle tip angle, the tip angle was held constant ($\theta_t = 20°$), whereas the cone half-angle was varied (Figure 5B). The dimensionless pressure drop for a cone half-angle $\theta_c = 5°$ is slightly larger than the others, but the three curves for θ_c = 10, 20, and 30° are nearly indistinguishable. In contrast, when cone half-angle is held constant ($\theta_c = 20°$) and tip angle is varied, the dimensionless pressure drop varies substantially with tip angle (Figure 5C), which is consistent with the expectation that pressure drop is controlled largely by fluid dynamics at the needle tip.

Possibly the most interesting aspect of the data in Figure 5C is that there is a minimum in the dimensionless pressure drop as a function of tip angle. For example, when Re = 1000, the minimum dimensionless pressure drop occurs when the tip angle is near $\theta_t = 20°$, which is when the microneedle has the profile of a straight-sided cone ($\theta_t = \theta_c$). The tip angle for minimum dimensionless pressure drop depends on the Reynolds number, such as $\theta_t \approx 30°$ when Re = 400 and $\theta_t \approx 40°$ when Re = 200. Almost identical results for the pressure drop occurred when other cone half-angles and needle lengths were considered, given that the pressure drop does not depend very strongly on these parameters (data not shown, but see above). The pressure drop is minimized when the needle is nearly a straight-sided cone because the flow is accelerated toward the tip in a manner that almost optimally reduces viscous boundary layer growth and losses, as discussed below. When $\theta_t < \theta_c$, the boundary layer grows more near the needle tip, which increases viscous friction and pressure drop in the microneedle. When $\theta_t > \theta_c$, viscous friction and pressure drop increase because of the more abrupt transition for the exit flow.

This same conclusion can be obtained by computing the dimensionless mass flow rate through the microneedle $\dot{m}$, defined as

$$\dot{m} = \frac{\dot{m}_a}{\rho A_t \sqrt{2\Delta p/\rho}} \tag{5}$$

where $\dot{m}_a$ is the dimensional mass flow rate, A_t is the tip area, and $\Delta p = p_0 - p_{atm}$ is the dimensional pressure drop across the microneedle. For four representative tip angles plotted in Figure 5C, the dimensionless mass flow rates are $\dot{m}$ = 0.7544, 0.8811, 0.8809, and 0.8494 corresponding to θ_t = 0, 20, 40, and 60°, respectively. The peak in the mass flow rate is rather broad, but the maximum value occurs near the tip angle of 20°, which corresponds to the geometry of a straight-sided cone ($\theta_t = \theta_c$).

Pressure profile along microneedle axis

Altogether, the results from Figures 4 and 5 show that the dimensionless pressure drop in a tapered microneedle depends weakly on the dimensionless length L, and the cone half-angle θ_c depends strongly on the tip angle θ_t, and is minimized when the needle profile is nearly a straight-sided cone ($\theta_t = \theta_c$). The reasons for this can be better understood by examining the pressure variation along the axis of the microneedle, which is most conveniently discussed in terms of a different scaling than that used for the dimensionless pressure drop ΔP defined in Eq. 4. This new dimensionless pressure is scaled with the total pressure drop across the microneedle as follows

$$P^* = \frac{p - p_{atm}}{p_o - p_{atm}} \tag{6}$$

Figure 6A shows this dimensionless pressure vs. the dimensionless distance x (nondimensionalized relative to needle tip diameter D_t) along the axis of the microneedle for four different tip angles, with constant cone half-angle $\theta_c = 20°$, dimensionless length $L = 10$, and Reynolds number Re = 500. Over 95% of the total pressure drop occurs in the last 40% of the length of the microneedle when $\theta_t = 0°$ and in the last 20% or less when $\theta_t \geq 20°$. These results show that the largest pressure variations in the microneedle are determined primarily by flow near the tip. In our model, tip geometry is strongly dependent on the tip angle θ_t and only weakly dependent on the dimensionless length L and cone half-angle θ_c, which explains why the tip angle is the primary parameter determining pressure variations in the microneedle.

The pressure profile in the microneedle for an incompressible, large-Reynolds-number flow (as shown in Figure 6A) is primarily an inviscid flow effect. As the cross-sectional area of the microneedle decreases, fluid velocity increases and pressure decreases. The inviscid portion of this pressure drop is a result of fluid acceleration. The viscous portion results from the growth of the viscous boundary layer along the wall of the microneedle. Near the tip of the microneedle, the large pressure variation causes a favorable pressure gradient that slows the growth of the boundary layer, thereby confining viscous effects closer to the wall and reducing the viscous portion of the pressure drop. However, if the tip angle is too large, the abrupt change in flow geometry at the tip introduces additional frictional effects that increase the viscous portion of the pressure drop (simulation data not shown).

The relative importance of viscous effects on pressure drop across a microneedle was determined using an inviscid flow model with a concentrated tip resistance. In this model, the flow is steady, the fluid density is constant, and the velocity is unidirectional and uniform across each cross section of the microneedle. The flow is inviscid from inside the plenum to just before the tip of the microneedle. The concentrated tip resistance produces a discrete pressure drop at the tip whose value is chosen so that the mass flow rate in the inviscid model is the same as that of the viscous flow in the numerical simulations for a given Reynolds number. Expressing the fluid velocity in the microneedle in terms of the mass flow rate and using Bernoulli's equation for the pressure give the following result for the scaled pressure profile

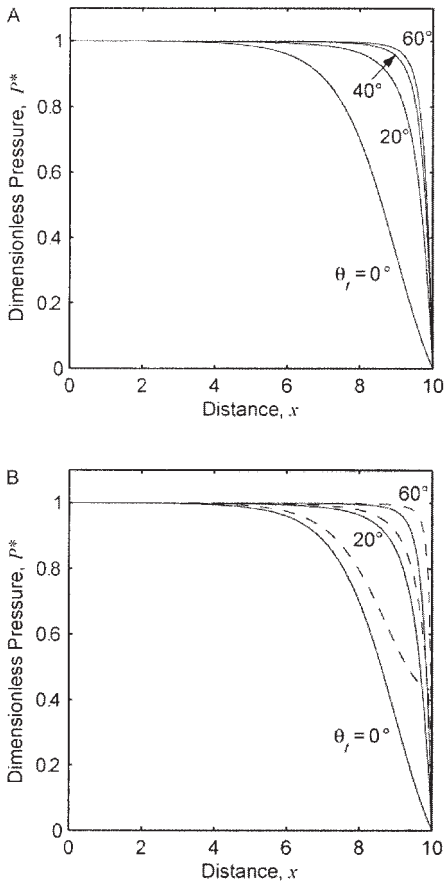

Figure 6. Scaled pressure *P (see text Eq. 6) vs. the dimensionless distance *x* along the axis for flow in microneedles.**

(A) The effect of tip angle $\theta_t = 0$, 20, 40, and 60°. The dimensionless pressure drops for these microneedles are $\Delta P = 1.757$, 1.288, 1.289, and 1.386, respectively. The dimensionless mass flow rates are $\dot{m} = 0.7544$, 0.8811, 0.8809, and 0.8494, respectively. (B) The effect of viscous losses. The solid lines are from the numerical simulations that include viscous and inertial effects, whereas the dashed lines are from the inviscid flow model with a tip resistance. The distance between the two curves in each pair represents the effect of viscous friction. These microneedles have tip angles $\theta_t = 0$, 20, and 60°. The dimensionless pressure drops for these microneedles are $\Delta P = 1.757$, 1.288, and 1.386, respectively. The dimensionless mass flow rates are $\dot{m} = 0.7544$, 0.8811, and 0.8494, respectively. All geometries have fixed Reynolds number Re = 500, cone half-angle $\theta_c = 20°$, and dimensionless length $L = 10$.

$$P^*(x) = 1 - \frac{\dot{m}^2}{D^4(x)} \tag{7}$$

where $D(x)$ is the dimensionless local diameter of the microneedle (scaled on the tip diameter D_t) and $\dot{m}$ is the dimensionless mass flow rate defined in Eq. 5. The largest dimensionless mass flow rate, $\dot{m}_{\max}$, occurs when the tip resistance is zero (that is, the flow is inviscid) and is independent of the shape or length of the microneedle. Viscous friction, as represented by the tip resistance, always decreases the flow rate.

Figure 6B shows a comparison of the pressure profiles in a microneedle obtained from the numerical simulations (solid curves) and from the inviscid flow model (dashed curves) for

Table 1. Parameters for Eq. 8, Which Correlates the Dimensionless Pressure Drop with the Reynolds Number as a Function of the Tip Angle θ_t

θ_t	K	a	b	c
0°	118.33	0.0181	1.065	0.435
5°	75.69	0.0280	1.040	0.408
10°	54.67	0.0372	1.029	0.399
15°	43.00	0.0447	1.007	0.412
20°	36.05	0.0496	0.969	0.452
25°	31.74	0.0514	0.922	0.518
30°	29.06	0.0507	0.877	0.607
35°	27.47	0.0486	0.839	0.710
40°	26.78	0.0459	0.810	0.816
45°	26.67	0.0435	0.791	0.912
50°	27.01	0.0417	0.779	0.993
55°	27.75	0.0407	0.772	1.053
60°	28.89	0.0404	0.767	1.094

three tip angles. The distance between the two curves for each tip angle represents the reduction in pressure caused by viscous friction. Viscous effects increase in magnitude and extend farther from the tip when the tip angle is close to zero. Viscous effects are minimized near the case of a straight-sided microneedle ($\theta_t = \theta_c = 20°$), as discussed earlier.

Statistical fit of simulation results to predict pressure drop

The results of these numerical simulations demonstrated that the dimensionless length L, the cone half-angle θ_c, and even the profile of the microneedle are not very important parameters in determining the overall pressure drop for flow through a microneedle, provided the cone half-angle θ_c is $\gtrsim$5 or 10°. This leaves the Reynolds number and the tip angle θ_t as the primary parameters needed to characterize the pressure drop, as shown in Figure 5C. To make these results more useful for the design of microneedles, simulation data from Figure 5C were fitted to the following functional form

$$\Delta P = \frac{K}{\mathrm{Re}}(1 + a\,\mathrm{Re}^b)^c + 1 \tag{8}$$

where K, a, b, and c are parameters that depend only on the tip angle θ_t. The values of these four parameters are given in Table 1 for microneedles with tip angles in the range $0 \le \theta_t \le 60°$, a cone half-angle $\theta_c = 20°$, and a dimensionless length $L = 10$. Over the Reynolds number range $0.1 \le \mathrm{Re} \le 1000$, this correlation is accurate with respect to the numerical results to $<1\%$ uncertainty for tip angles in the range $0° \le \theta_t \le 35°$ and to no more than 1.7% for tip angles in the range $35° < \theta_t \le 60°$. For the restricted dimensionless pressure drop range $1 \le \Delta P \le 2$, the correlation is accurate to $<0.5\%$ for tip angles in the range $0° \le \theta_t \le 30°$ and to no more than 1% for tip angles in the range $30 < \theta_t \le 60°$.

Discussion

Overall, the experimental data from this study of conically tapered microneedles were consistent with the well-known behavior of internal flows. When all of the pressure-drop data for different needle geometries and fluid viscosities were nondimensionalized, they collapsed into a set of similar curves that were a function of the Reynolds number (Figure 3B). These curves exhibited the characteristic creeping-flow limit at small Reynolds number, in which the dimensionless pressure drop is inversely proportional to the Reynolds number, and the characteristic inviscid-flow limit at large Reynolds number, in which the dimensionless pressure is independent of Reynolds number.

Numerical simulations revealed additional complexities to the flow arising from the needle's tapered geometry and short length. The most significant finding is that the pressure drop required to flow fluid through a microneedle is controlled primarily by the tip angle θ_t (Figure 5) and tip diameter D_t (found in the Reynolds number). This is because the microneedle flows in this study were not fully developed. Each microneedle was so short that the viscous boundary layer on the interior wall did not grow to the point of merger. This behavior was also aided by the tapered geometry that created a favorable axial-pressure gradient that inhibited boundary-layer growth. The numerical simulations further showed that the pressure drop across the microneedle was minimized when its geometry was near that of a straight-sided cone.

Agreement between our experimental data and numerical simulations is good (MAPE = 11%). The discrepancies are most probably the result of our idealization of microneedle geometry as a straight-sided cone. Because of the limitations of fabrication and measurement at the micron scale, actual microneedles did not always have perfectly circular cross sections and needle diameters were estimated with an experimental uncertainty of about ± 3 μm (data not shown). Microneedles were not uniformly tapered either, often exhibiting a "Coke® bottle" shape (Figure 1B). Although the simulations could account for some curvature in the needle taper, we did not simulate the complex curvature of these actual microneedles. As discussed above, such inaccuracies in the representation of the needle-tip geometry would then be a major factor contributing to the discrepancies between simulations and experiments. Finally, microneedle walls had surface roughness features on the order of 0.1 μm (data not shown). Simulations assumed smooth walls.

This study was motivated by applications in drug delivery and microfluidics. The observation that tip geometry generally controls flow within tapered microneedles provides significant flexibility in needle design. This is important when balancing design constraints to make needles that have the appropriate geometry and material properties to insert into skin without breaking or bending, avoid causing pain, and inject useful quantities of drug. We also observed that only kilopascal pressure drops were needed to flow many microliters per second through a micron-scale needle. Battery-powered micropumps in a handheld or wearable device could easily apply such pressures and achieve flow rates of medical significance, especially if multineedle arrays were used to increase throughput and add redundancy. Not considered in this analysis is the resistance to fluid dispersion in the tissue into which a microneedle injection might be performed. Based on our preliminary measurements, this resistance can be considerable (data not shown) and, given the relatively low pressure drops across microneedles, tissue resistance is likely to be the dominant resistance to flow during a microneedle injection into skin.

Conclusions

To develop microneedles for painless injection and other microfluidic applications, we experimentally determined the relationship between pressure drop and flow rate as a function of microneedle geometry and fluid viscosity. Pressure drops in the range of 4.6–196.5 kPa were sufficient to flow liquids at rates of 1.4–56 μL/s, which suggests that micropumps could be used to deliver medically useful quantities of fluid from a patchlike device. Numerical simulation showed that needle tip diameter and tip angle are the primary control parameters for flow through conically tapered microneedles, whereas other geometric features, such as needle length and inlet diameter, are much less important. The curvature of the taper also plays a small role, with straight-sided needles exhibiting the least resistance to flow stemming from the nearly optimal development of the viscous boundary layers for this geometry and range of Reynolds numbers. Altogether, the experimental and numerical results from this work suggest that a microneedle designed to deliver a maximum flow rate with minimum pressure drop would have the shape of a straight-sided cone with a cone half-angle of about 20–30° and a large tip diameter. This work also shows that fluid can flow through microneedles for drug delivery and other microfluidic applications with only modest pressure drops that can be predicted and optimized using a numerical model.

Acknowledgments

We thank Mark Allen, Shawn Davis, Esi Ghartey-Tagoe, Suo Jin, and Yangqing Xu for technical assistance and helpful discussions. This work was supported in part by the American Diabetes Association and the National Institutes of Health.

Literature Cited

1. Park K, ed. *Controlled Drug Delivery: Challenges and Strategies*. Washington, DC: American Chemical Society; 1997.
2. Langer R. Drug delivery and targeting. *Nature Suppl.* 1998;392:5-10.
3. Prausnitz MR. Overcoming skin's barrier: The search for effective and user-friendly drug delivery. *Diabetes Technol Ther*. 2001;3:233-236.
4. Amsden BG, Goosen MFA. Transdermal delivery of peptide and protein drugs: An overview. *AIChE J*. 1995;41:1972-1997.
5. Bronaugh RL, Maibach HI, eds. *Percutaneous Absorption: Drugs—Cosmetics—Mechanisms—Methodology* New York, NY: Marcel Dekker; 1999.
6. Barry BW. Novel mechanisms and devices to enable successful transdermal drug delivery. *Eur J Pharm Sci*. 2001;14:101-114.
7. Henry S, McAllister DV, Allen MG, Prausnitz MR. Microfabricated microneedles: A novel approach to transdermal drug delivery. *J Pharm Sci*. 1998;87:922-925.
8. McAllister DV, Allen MG, Prausnitz MR. Microfabricated microneedles for gene and drug delivery. *Annu Rev Biomed Eng*. 2000; 2:289-313.
9. McAllister DV, Wang PM, Davis SP, Park JH, Canatella PJ, Allen MG, Prausnitz MR. Microfabricated needles for transdermal delivery of macromolecules and nanoparticles: Fabrication methods and transport studies. *Proc Natl Acad Sci USA*. 2003;100:13755-13760.
10. Kaushik S, Hord AH, Denson DD, McAllister DV, Smitra S, Allen MG, Prausnitz MR. Lack of pain associated with microfabricated microneedles. *Anesth Analg*. 2001;92:502-504.
11. Matriano JA, Cormier M, Johnson J, Young WA, Buttery M, Nyam K, Daddona PE. Macroflux® microprojection array patch technology: A new and efficient approach for intracutaneous immunization. *Pharm Res*. 2002;19:63-70.
12. Mikszta JA, Alarcon JB, Brittingham JM, Sutter DE, Pettis RJ, Harvey NG. Improved genetic immunization via micromechanical disruption of skin-barrier function and targeted epidermal delivery. *Nat Med*. 2002;8:415-419.
13. McAllister, DV, Cros F, Davis SP, Matta LM, Prausnitz MR, Allen MG. Three-dimensional hollow microneedle and microtube arrays [abstract]. Proc of Transducers '99: 10th Int Conf on Solid-State Sensors and Actuators; 2000:1098-1101.
14. Davis SP, Prausnitz MR, Allen MG. Fabrication and characterization of laser micromachined hollow microneedles [abstract]. Proc of Transducers '03: 12th Int Conf on Solid-State Sensors, Actuators, and Microsystems; 2003:1435-1438.
15. Davis SP, Landis BJ, Adams ZH, Allen MG, Prausnitz MR. Insertion of microneedles into skin: measurement and prediction of insertion force and needle fracture force. *J Biomech.* 2004;37:1155-1163.
16. Stoeber B, Liepmann D. Fluid injection through out-of-plane microneedles [abstract]. Proc of 1st Annual Int IEEE-EMBS Special Topic Conf on Microtechnologies in Medicine & Biology; 2000:224-228.
17. Gardeniers HJGE, Luttge R, Berenschot EJW, de Boer MJ, Yeshurun SY, Hefetz M, van't Oever R, van den Berg A. Silicon micromachined hollow microneedles for transdermal liquid transport. *J Microelectromech Syst*. 2003;12:855-862.
18. Trebotich D, Zahn JD, Prabhakarpandian B, Liepmann D. Modeling of microfabricated microneedles for minimally invasive drug delivery, sampling and analysis. *Biomed Microdev*. 2003;5:245-251.
19. Stone HA, Kim S. Microfluidics: Basic issues, applications, and challenges. *AIChE J*. 2001;47:1250-1254.
20. Oka S. The steady slow motion of a viscous fluid through a tapered tube. *J Phys Soc Jpn*. 1964;19:1481-1484.
21. Sutterby JL. *Laminar Newtonian and Non-Newtonian Converging Flow in Conical Sections*. PhD Dissertation. Madison, WI: University of Wisconsin; 1964.
22. Nishimura J, Oka S. The steady flow of a viscous fluid through a tapered tube. *J Phys Soc Jpn*. 1965;20:449-453.
23. Kwon TH, Shen SF, Wang KK. Pressure drop of polymeric melts in conical converging flow: Experiments and predictions. *Polym Eng Sci*. 1986;26:214-224.
24. Kemblowski Z, Kiljanski T. Flow of Stokesian fluids through conical ducts. *Chem Eng J*. 1975;9:141-151.
25. Jarzebski AB, Wilkinson WL. Non-isothermal developing flow of a generalised power-law fluid in a tapered tube. *J Non-Newtonian Fluid Mech*. 1981;8:239-248.
26. Garrioch SH, James DF. A finite-element study of Newtonian and power-law fluids in conical channel flow. *J Fluids Eng*. 1997;119:341-346.
27. Sushil S, Peach JP, Hitt DL, Eggleton CD. Rheology of mixtures of artificial blood and erythrocyte suspensions [abstract]. Proc of ASME Bioengineering Conf 2001;50:481-482. Available at: http://asme.pinetec.com/bio2001/data/pdfs/a0180665.pdf. Accessed May 26, 2004.
28. Harrison WJ. The pressure in a viscous liquid moving through a channel with diverging boundaries. *Proc Cambridge Phil Soc*. 1919; 19:307-312.
29. Munson BR, Young DF, Okiishi TH. *Fundamentals of Fluid Mechanics*. 4th Edition. Hoboken, NJ: Wiley; 2002:448,457.

Manuscript received May 27, 2004, and revision received Oct. 22, 2004.